

Verification and Validation

Computer simulations are in many engineering applications a cost-efficient way of conducting design and performance optimization of physical problems. But blindly trusting numbers generated from a computer code can prove to be naive. It doesn't take a lot of coding experience before one realizes many things that can break down and produce unwanted or unexpected results. Therefore, credibility of computational results are essential, meaning the simulation is worthy of belief or confidence [26]. Verification and validation (V&V) is the main approach for assessing the reliability of computational simulations [38]. A thorough discussion of (V&V) concepts and terminology can be found in [26]. In this thesis, the definitions provided by the *American Society of Mechanical Engineers guide for Verification and Validation in Computational Solid Mechanics* [35] are followed:

Definition 4.1. Verification: The process of determining that a computational model accurately represents the underlying mathematical model and its solution.

Definition 4.2. Validation: The process of determining the degree to which a model is an accurate representation of the real world from the perspective of the intended uses of the model.

Simplified, *verification* considers if one solves the equations right, while *validation* is checking if one solves the right equations for the given problem [32]. To test a computational code for all possible parameters, conditions, and applications, are simply too time consuming. Verification and validation is therefore ongoing processes, with no clear boundary of completeness unless additional requirements are specified [32]. The goal of this chapter is to verify the implementations using the method of manufactured solution (MMS), addressing validation in a subsequent chapter.

4.1 Verification of Code

Within scientific computing a mathematical model is often the baseline for simulations of a particular problem of interest. For scientists exploring physical phenomena, the mathematical model is often in the form of systems of partial differential equations (PDEs). Through verification of code, the ultimate goal is to ensure a computer program truly represents the mathematical model. To accumulate sufficient evidence that a mathematical model is solved correctly by a computer code,

it must excel within predefined criteria. If the acceptance criterion is not satisfied, a coding mistake is suspected. Should the code pass the preset criteria, the code is considered verified. Of the different classes of test found in [32], *Order-of-accuracy (OAA)* is regarded as the most rigorous ~~acceptance criterion for verification~~ [34, 32, 6]. The method tests if the discretization error E is reduced in coordination with the *formal order of accuracy* expected from the numerical scheme. The formal order of accuracy is defined to be the theoretical rate at which the truncation error of a numerical scheme is expected to reduce. The *observed order of accuracy* is the actual rate produced by the numerical solution. For order of convergence tests, the code is assumed to be verified if the observed discretization error is proportional to the formal order of accuracy. Monitoring the discretization error E by spatial and temporal refinements, one assumes the error E can be expressed as,

$$E = C\Delta t^p + D\Delta x^l$$

where C and D are constants, Δt and Δx represents the spatial and temporal resolution, while p and l is the observed order of accuracy of the numerical scheme. If Δt small compared to Δt , the spatial discretization error can be neglected, which can use that to find l , which is the observed order of convergence for the temporal discretization error. To calculate the error, E , an exact/reference solution is needed which rarely exist for complex mathematical models. The next subsection presents an efficient method for generating such solutions.

4.1.1 Method of manufactured solution

The basis of a convergence test is to find an exact/reference solution, to compute the discretization error E . However, solutions of PDEs are limited, and simplifications of the original problem are often necessary to produce analytical solutions. The *method of manufactured solutions* provides a simple yet robust way of ~~making~~ analytic solutions for PDEs. Let a ~~partial~~ differential equation of interest be on the form

$$\mathbf{L}(\mathbf{u}) = \mathbf{f}$$

Here \mathbf{L} is a differential operator, \mathbf{u} is variable the of interest, and \mathbf{f} is some sourceterm. In MMS, one first manufactures a solution \mathbf{u} for the given problem, producing a sourceterm \mathbf{f} after differentiation by \mathbf{L} . The produced source term will cancel any imbalance formed by the manufactured solution \mathbf{u} of the original problem. Therefore, the manufactured solution can be constructed without any physical reasoning, proving code verificaion as a purely a mathematical exercise were the only interest is to verify the solution [31].

If the MMS is not chosen properly, the test will not work. Therefore some guidelines for rigorous verification have been proposed in [6, 34, 31]:

- The manufactured solution (MMS), should be composed of smooth analytic functions such as exponential, trigonometric, or polynomials.
- The MS should have sufficient number of derivatives, exercising all terms and derivatives of the PDEs.

To properly verify the robustness of the method of manufactured solution, a report regarding code verification through MMS for the time-dependent Navier-Stokes equation was published by Salari and Knupp [34]. To prove its robustness, the authors deliberately implemented code errors in a verified Navier-Stokes solver through MMS. In total 21 blind test-cases were implemented, where different approaches of verification frameworks were tested. Of these, 10 coding mistakes that reduced the observed order-of-accuracy were implemented. The MMS captured all coding mistakes, except one. This mistake would, according to the author, have been captured if his guidelines for conducting MMS had been followed.

In general, computing the source term \mathbf{f} can be quite challenging and error prone. Therefore, symbolic computation of the source term is advantageous to overcome mistakes which can easily occur when calculating by hand. For construction of the source term \mathbf{f} , the Unified Form Language (UFL) [1] provided in FEniCS Project will be used. COMPUTE VV HERE

4.1.2 Comment on verification of the fluid-structure interaction solver by MMS

In general the MMS does not need to match any physical processes. However, when considering multiphysics problems, such as FSI, the equations have to meet the mathematical criteria from Section 3.2:

Let $\hat{\mathbf{v}}_s, \hat{\mathbf{v}}_f$ be the structure and fluid velocity, and let σ_s, σ_f be the Cauchy stress tensor for the structure and fluid respectively. Let \mathbf{n}_i be the normal vector pointing out of the domain i . We then have the following interface boundary conditions.:

1. Kinematic boundary condition $\hat{\mathbf{v}}_s = \hat{\mathbf{v}}_f$, enforced strongly by a continuous velocity field in the fluid and solid domain.
2. Dynamic boundary condition $\sigma_s \cdot \mathbf{n}_s = \sigma_f \cdot \mathbf{n}_f$, enforced weakly by omitting the boundary integrals from the weak formulation in problem.

The choice of a MMS is therefore not trivial, as it must fulfill condition 1 and 2, in addition to the divergence-free condition in the fluid, and avoiding cancellation of the ALE-convective term $\frac{\partial \hat{\mathbf{T}}_f}{\partial t}$. The construction of a MMS for a monolithic FSI problem is therefore out of the scope of this thesis. The struggle is reflected of the absence of research, regarding MMS for coupled FSI solvers in the literature. The challenge is often disregarded, such as [36], where the verification process is

conducted on the fluid and structure solver separately. Instead, the accuracy of the coupling is evaluated by the code validation. The approach clearly ease the process, assuming verification of each codeblock is "sufficient" to declare the code verified. In this thesis, the approach found in [36] was followed, but it must be stressed that solving each problem individually is not true verification, ~~in reference to a monolithic approach where the problems are simultaneously~~.

4.2 Validation of Code

Through *verification*, one can assure that a scientific code evaluate mathematical model correctly. However, accuracy is unnecessary if the model fails to serve as an appropriate representation of the physical problem. By definition 4.2, *Validation* is the act of demonstrating that a mathematical model is applicable for its intended use with a certain degree of accuracy. That is, a mathematical model is validated if it meets some predefined criteria within a specific context. Validation is therefore not intended to portray the model as an absolute truth, nor the best model available [33]. In scicomp., validation is conducted by comparing numerical results against existing experimental data. The design of validation experiments vary by the motivation of the creators, where validated experiments for computational science can be divided into three groups [38]: (1)To improve fundamental understanding of a physical process, (2)Discovery or enhancement of mathematical models of well known physical processes, (3)To conclude the reliability and performance of systems. The assessment of comparison between numerical results and experimental data, makes *validation* assess a wide range of issues [38]. Is the experiment relevant, and conducted correctly in accordance with prescribed parameters? What about the measurement uncertainty of reference experimental data? These issues must be addressed in order to raise sufficient confidence that the mathematical model is credible for its intended use.

4.3 Validation benchmark

The numerical benchmark presented in [16] has been chosen for validation of the *One-step θ* scheme from chapter 3. The benchmark has been widely accepted as a rigid validation benchmark throughout the litterature [48, 50, 43, 12]. This is mainly due to the diversity of tests included, challenging all the main components of a fluid-structure interaction scheme. The benchmark is based on the *von Kármán vortex street* [46], where a cylinder is placed off-center in a 2D channel. In [16], an additional elastic flag is placed behind the cylinder, see Figure 4.1

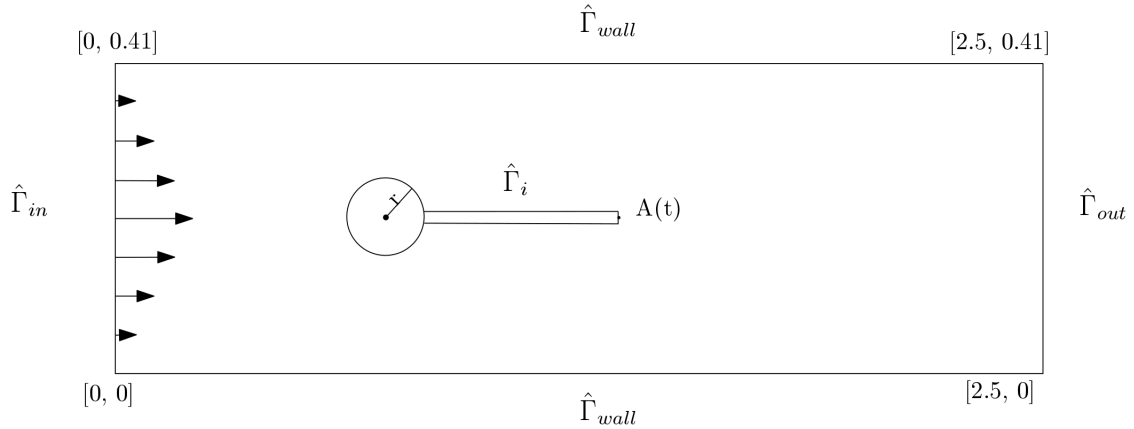


Figure 4.1: Computational domain of the validation benchmark

The benchmark is divided into three problems, each further divided into three different sub-problems with increasing complexity. In the first problem, the fluid solver is tested for a series of different flow profiles. The second branch considers the structure solver, regarding bending of the elastic flag. And the final branch concerns validation of a full fluid-structure interaction problem with the fluid and the elastic flag. Several quantites for comparison are presented in [16] for validation purposes:

- The position (x,y) of point $A(t)$ as the elastic flag undergoes deformation.
- Drag and lift forces exerted on of the whole interior geometry in contact with the fluid, consisting of the rigid circle and the elastic beam.

$$(F_D, F_L) = \int_{\Gamma} \sigma \cdot \mathbf{n} dS$$

All problems pose both steady state and periodic solutions. For the steady state solutions, the quantity of interest will be calculated based on a transient simulation, that has converged towards a steady state solution. For the periodic solutions, the amplitude and mean values for the time dependent quantity are calculated from the last period.

$$\text{mean} = \frac{1}{2} \max + \min \quad (4.1)$$

$$\text{amplitude} = \frac{1}{2} \max - \min \quad (4.2)$$

In [16], all steady state solutions seems to be calulated by solving a steady state equation since time-step are only reported for the periodic solutions. In this thesis, all problems in [16] are calculated using time integration. The main reason for solving the problem transiently rather than steady state, is that numerical errors associated with initial transients are negligible with a sufficiently low time step size, without laborious changes to the numerical implementation. In the following section, an overview of each problem together with numerical results will be presented. A discussion of the results are given at the end of each simulation brancht. For each table, the relative error of the finest spatial and temporal refinement compared to the reference solution is reported in [16].

4.3.1 Validation of fluid solver

The validation of the fluid solver concerns transient flow for a low Reynold-number regime. Two approaches for the validation are given in [16]. The first approach considers the setup as a fluid-structure interaction problem, setting the elastic flag close to rigid by manipulation of the structure parameters. In the second approach, the flag is set fully rigid and considered a purely flow problem, meaning any influence of the structure and mesh moving model is eliminated. Hence, no deformation of the fluid domain occurs, and the fluid problem can be defined in an Eulerian description of motion.

Let \mathbf{v}_f , p_f be the fluid velocity and pressure, and let σ_f be the Cauchy stress tensor, and \mathbf{f}_f denote any sourceterm, Find \mathbf{v}_f , p_f such that :

$$\begin{aligned} \left(\frac{\partial \mathbf{v}_f}{\partial t}, \psi^u \right)_{\hat{\Omega}_f} + ((\mathbf{v}_f \cdot \nabla) \mathbf{v}_f, \psi^u)_{\Omega_f} - (\hat{\sigma}, \nabla \psi^u)_{\Omega_f} - (\rho_f \mathbf{f}_f, \psi^u)_{\Omega_f} &= 0 \\ (\nabla \cdot \mathbf{v}_f), \psi^p)_{\Omega_f} &= 0 \end{aligned}$$

parameter	CFD-1	CFD-2	CFD-3
$\rho^f [10^3 \frac{kg}{m^3}]$	1	1	1
$\nu^f [10^{-3} \frac{m^2}{s}]$	1	1	1
U	0.2	1	2
Re	20	100	200

Table 4.1: Fluid sub-problem parameters

The validation of the fluid solver is divided into three sub-problems; CFD-1, CFD-2, and CFD-3, each with different fluid parameters shown in Table 4.1. While CFD-1 and CFD-2 yields steady state solutions, CFD-3 is a periodic solution. A parabolic velocity profile on the form,

$$v_f(0, y) = 1.5U \frac{(H - y)y}{(\frac{H}{2})^2}$$

is set on the left channel inflow. H is the height of the channel, while the parameter U is set differently to each problem to induce different inlet flow profiles. At the right channel outflow, the pressure is set to $p = 0$. No-slip boundary conditions for the fluid are enforced on the channel walls, and on the inner geometry consisting of the circle and the elastic flag. The validation of the fluid solver is based on the evaluation of drag and lift forces on the inner geometry, compared against a reference solution. A spatial and temporal convergence study is conducted on all sub-problems.

Results

Table 4.2, 4.3, and 4.4 below shows the numerical solution of each sub, CFD-1, CFD-2, and CFD-3. Each sub-problem is evaluated on four different mesh with increasing resolution. For the numerical solution of CFD-3 in Table 4.4, additional temporal and spatial refinement studies are conducted. Figure 4.1 shows the evaluation of lift and drag for the finest spatial and temporal resolution, while Figure 4.3 shows a visual representation of the fluid flow through the channel.

$\Delta t = 0.1 \theta = 1.0$			
nel	ndof	Drag	Lift
1438	6881	13.60	1.089
2899	13648	14.05	1.126
7501	34657	14.17	1.109
19365	88520	14.20	1.119
Reference		14.29	1.119
Error		0.006 %	0.00 %

Table 4.2: CFD-1 results, lift and drag evaluated at the inner geometry surface for increasing spatial refinement. The error is computed as the relative error from the highest mesh resolution against the reference solution.

$\Delta t = 0.01 \ \theta = 1.0$			
nel	ndof	Drag	Lift
1438	6881 (P2-P1)	126.0	8.62
2899	13648 (P2-P1)	131.8	10.89
7501	34657 (P2-P1)	135.1	10.48
19365	88520(P2-P1)	135.7	10.55
Reference		136.7	10.53
Error		0.007 %	0.001 %

Table 4.3: CFD-2 results, lift and drag evaluated at the inner geometry surface for increasing spatial refinement. The error is computed as the relative error from the highest mesh resolution against the reference solution.

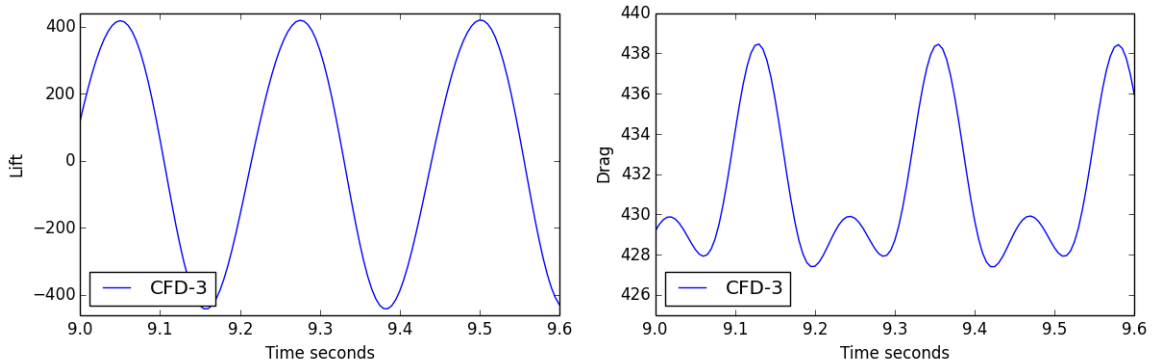


Figure 4.2: CFD-3, lift and drag forces at time $t = [9, 9.6]$.

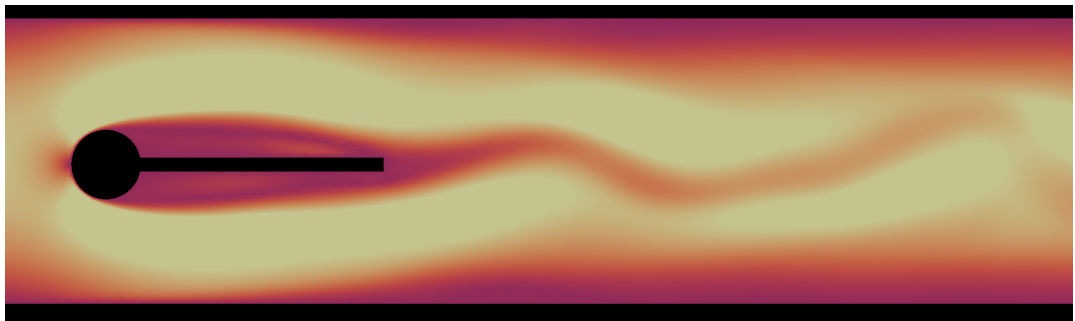


Figure 4.3: CFD-3, flow visualization of velocity time $t = 9s$.

$\Delta t = 0.01 \ \theta = 0.5$			
nel	ndof	Drag	Lift
1438	6881 (P2-P1)	417.23 ± 0.0217	-249.21 ± 0.32
	16474 (P3-P2)	414.86 ± 5.6282	-7.458 ± 444.07
2899	13648 (P2-P1)	408.50 ± 4.3029	-19.731 ± 373.45
	32853 (P3-P2)	432.86 ± 5.5025	-9.686 ± 431.28
7501	34657 (P2-P1)	431.57 ± 5.2627	-12.497 ± 429.76
	83955 (P3-P2)	438.20 ± 5.5994	-11.595 ± 438.00
19365	88520 (P2-P1)	435.43 ± 5.4133	-11.545 ± 438.89
	215219 (P3-P2)	438.80 ± 5.6290	-11.158 ± 439.23
Reference		439.95 ± 5.6183	-11.893 ± 437.81
Error		$0.002 \% \pm 0.001 \%$	$0.061 \% \pm 0.003\%$
$\Delta t = 0.005 \ \theta = 0.5$			
nel	ndof	Drag	Lift
1438	6881 (P2-P1)	417.24 ± 0.0084	-249.386 ± 0.1345
	16474 (P3-P2)	414.90 ± 5.7319	-8.467 ± 443.45
1438	13648 (P2-P1)	408.27 ± 4.0192	-18.981 ± 363.84
	32853 (P3-P2)	432.90 ± 5.5333	-11.382 ± 430.60
1438	34657 (P2-P1)	431.59 ± 5.2979	-13.644 ± 429.68
	7501	438.23 ± 5.6393	-12.917 ± 437.78
1438	88520 (P2-P1)	435.46 ± 5.4579	-13.190 ± 438.05
	19365	438.84 ± 5.6576	-12.786 ± 438.36
Reference		439.95 ± 5.6183	-11.893 ± 437.81
Error		$0.002 \% \pm 0.006 \%$	$0.075 \% \pm 0.001\%$

Table 4.4: CFD-3 results, lift and drag evaluated at the inner geometry surface. A spatial refinement study is conducted for increasing mesh resolution and two different finite element pairs. The relative error is computed from the solution of the highest mesh resolution, against the reference solution.

The numerical solutions of CFD-1 in Figure 4.2 shows convergence against the reference solution. Choosing P2-P1 elements together with a fully implicit scheme $\theta = 1$, a relative error of 0.006% for lift, and 0% for drag is attained. For the numerical solution of CFD-2 presented in Figure 4.3, the same observations apply. The second order Crank–Nicolson scheme $\theta = 0.5$ was investigated for CFD-1 and CFD-2, however only improving the results of order 10^{-6} for both lift and drag. For the periodic problem CFD-3, the choice of P2-P1 elements with a fully implicit time-stepping scheme proved insufficient for capturing the expected periodic solution. Using Crank–Nicolson time-stepping scheme $\theta = 0.5$, the periodic solution was attained.

Discussion

Since the choice of finite-element pair is not reported in the original work, both P3-P2 and P2-P1 element pairs for fluid and pressure respectively was compared in combination with spatial mesh refinement. From Table 4.3, a relative error < 0.08% of the mean and amplitude for lift and drag is attained. The choice P3-P2 element pair is eminent to achieve reasonable results for the first and second mesh regardless of time step. However, the third and fourth mesh resolution shows close resemblance with the reference solution, independent of finite-element pair. On basis of the presented results, the fluid solver is validated in accordance with the proposed benchmark.

4.3.2 Validation of solid solver

The validation of the solid solver is conducted on a rectangular domain, representing the elastic structure in Figure 4.1. The structure is fixed to a fictional wall on the left side of the domain, pulled by a gravitational force $\mathbf{g} = (0, g)$. The validation of the solid solver is based on comparison of the deflection of point $A(t) = [A_x(t), A_y(t)]$, conducted on three refined mesh, where the number of finite elements are chosen in close resemblance with the original work in [16]. A simple investigation of different finite-element pairs, suggest that P3-P3 elements where used for making the reference solution. In this study, lower order finite-element pair was included, comparing shorter simulation time with solution accuracy. While computational time is not a major concern for the solid solver, the study is important for potentially reducing the computational time for the final validation branch

parameter	CSM 1	CSM 2	CSM 3
$\rho^s [10^3 \frac{kg}{m^3}]$	1	1	1
ν^s	0.4	0.4	0.4
$\mu^s [10^6]$	0.5	2.0	0.5
$g \frac{m}{s^2}$	2.0	2.0	2.0

Table 4.5: Solid sub-problem parameters

Results

The numerical results for CSM-1, CSM-2, and CSM-3 are presented in table Table 4.6, 4.7, 4.8, and 4.9. For the steady state sub-problems CSM-1 and CSM-2, a spatial convergence study is conducted through mesh refinement with three different finite-element pairs. For the periodic CSM-3 problem, an additional temporal study was conducted for two different time steps. In Figure 4.4, a visualization of CSM-3 is provided for three different time steps. Finally, Figure 4.5 shows the displacement vector components, comparing all finite-element pairs for the finest mesh resolution.

For CSM-1, the relative error of deformation found in Table 4.6, is 1.41% and 0.8% for the x and y coordinate respectively. In Table 4.7, a relative error of 1.49% and 0.88% for the x,y components can be found for CSM-2, proving both steady state problems coincide with the reference solution. In Table 4.8, the numerical solutions CSM-3 for time steps $\Delta t = 0.01$ and $\Delta t = 0.005$, are in close resemblance with the reference solution. The study of lower-order elements proved successful for all problems, justifying accurate results can be achieved using P2-P2 elements for deformation and velocity, even for coarse mesh resolution.

$\Delta t = 0.1 \theta = 1.0$			
nel	ndof	ux of A [$x 10^{-3}$]	uy of A [$x 10^{-3}$]
319	832 P1-P1	-5.278	-56.6
	2936 P2-P2	-7.056	-65.4
	6316 P3-P3	-7.064	-65.5
1365	3140 P1-P1	-6.385	-62.2
	11736 P2-P2	-7.075	-65.5
	25792 P3-P3	-7.083	-65.5
5143	11084 P1-P1	-6.905	-64.7
	42736 P2-P2	-7.083	-65.4
	94960 P3-P3	-7.085	-65.5
Reference		-7.187	-66.1
Error		1.41 %	0.8 %

Table 4.6: CSM-1, deformation components of $A(t)$ for $\Delta t = 0.1$ and increasing spatial refinement. The error is computed as the relative error from the highest mesh resolution against the reference solution.

$\Delta t = 0.05 \theta = 1.0$			
nel	ndof	ux of A [$x 10^{-3}$]	uy of A [$x 10^{-3}$]
319	832 P1-P1	-0.3401	-14.43
	2936 P2-P2	-0.460	-16.78
	6316 P3-P3	-0.461	-16.79
1365	3140 P1-P1	-0.414	-15.93
	11736 P2-P2	-0.461	-16.81
	25792 P3-P3	-0.461	-16.82
5143	11084 P1-P1	-0.449	-16.60
	42736 P2-P2	-0.461	-16.82
	94960 P3-P3	-0.462	-16.82
Reference		-0.469	-16.97
Error		1.49%	0.88 %

Table 4.7: CSM-2, deformation components of $A(t)$ for $\Delta t = 0.05$ and increasing spatial refinement. The error is computed as the relative error from the highest mesh resolution against the reference solution.

$\Delta t = 0.01 \theta = 0.5$			
nel	ndof	ux of A [$x 10^{-3}$]	uy of A [$x 10^{-3}$]
319	832 P1-P1	-10.835 +/- 10.836	-55.197 +/- 56.845
	2936 P2-P2	-14.390 +/- 14.392	-63.303 +/- 65.149
	6316 P3-P3	-14.432 +/- 14.435	-63.397 +/- 65.263
1365	3140 P1-P1	-13.053 +/- 13.054	-60.367 +/- 62.241
	11736 P2-P2	-14.428 +/- 14.432	-63.388 +/- 65.256
	25792 P3-P3	-14.444 +/- 14.446	-63.432 +/- 65.287
5143	11084 P1-P1	-14.082 +/- 14.084	-62.656 +/- 64.495
	42736 P2-P2	-14.444 +/- 14.447	-63.435 +/- 65.288
	94960 P3-P3	-14.449 +/- 14.452	-63.449 +/- 65.296
Reference		-14.305 +/- -14.305	-63.607 +/- 65.160
Error		1% \pm 1%	0.24% \pm 0.24%

Table 4.8: CSM-3, deformation components of $A(t)$ for $\Delta t = 0.01$, with increasing temporal refinement. The error is computed as the relative error from the highest mesh resolution.

$\Delta t = 0.005 \theta = 0.5$			
nel	ndof	ux of A [$x 10^{-3}$]	uy of A [$x 10^{-3}$]
319	832 P1-P1	-10.846 +/- 10.848	-56.049 +/- 56.053
	2936 P2-P2	-14.390 +/- 14.391	-63.738 +/- 64.703
	6316 P3-P3	-14.429 +/- 14.430	-63.833 +/- 64.810
1365	3140 P1-P1	-13.057 +/- 13.057	-60.813 +/- 61.826
	11736 P2-P2	-14.426 +/- 14.427	-63.827 +/- 64.801
	25792 P3-P3	-14.440 +/- 14.441	-63.854 +/- 64.845
5143	11084 P1-P1	-14.091 +/- 14.091	-63.195 +/- 63.981
	42736 P2-P2	-14.441 +/- 14.441	-63.856 +/- 64.847
	94960 P3-P3	-14.446 +/- 14.446	-63.865 +/- 64.860
Reference		-14.305 +/- -14.305	-63.607 +/- 65.160
Error		1% \pm 1%	0.4% \pm 0.4%

Table 4.9: CSM-3, deformation components of $A(t)$ for $\Delta t = 0.005$, with increasing temporal refinement. The error is computed as the relative error from the highest mesh resolution.

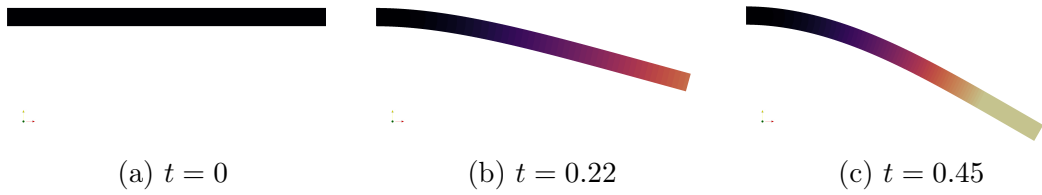


Figure 4.4: CSM-3, visualization of deformation of the elastic flag for three time steps: (a) initial configuration, (b) half way extension, (c) full extension

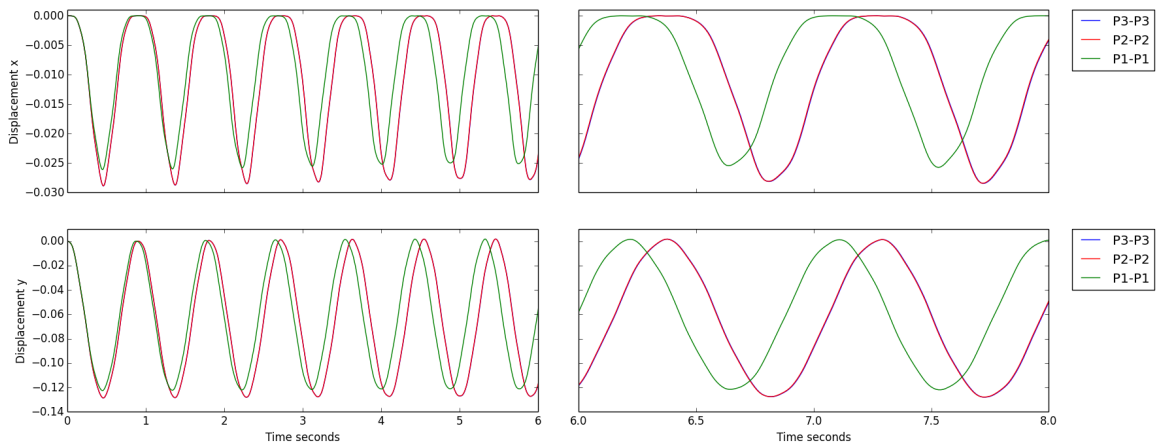


Figure 4.5: CSM-3 $\Delta t = 0.01$, deformation components of $A(t)$ with finest mesh resolution, comparing all finite element pairs for time interval $t \in [0, 6]$ and $t \in [6, 8]$.

Discussion

Comparing all finite-element pairs for CSM-3, visualized in figure 4.5, shows P2-P2 and P3-P3 elements hardly can be distinguished from each other. In accordance with previous mentioned results and observations, the solid solver is validated in accordance with the validation benchmark.

4.3.3 Validation of fluid structure interaction solver

The validation of the FSI solver consist of three sub-problems which will be referred to FSI-1, FSI-2 and FSI-3. The FSI-1 problem yields a steady state solution for the system, inducing small deformations to the elastic flag. The FSI-2 and FSI-3 problems results in a periodic solution, where the elastic flag oscillates behind the cylinder. All sub-problems inherit the conditions from the previous validation branches, with the exception of no gravitational force on the elastic flag. On the fluid-structure interface Γ , we enforce the kinematic and dynamic boundary condition

$$\mathbf{v}_f = \mathbf{v}_s \quad (4.3)$$

$$\boldsymbol{\sigma}_f \cdot \mathbf{n} = \boldsymbol{\sigma}_s \cdot \mathbf{n} \quad (4.4)$$

Apart from the accuracy of the reported values, the main purpose of the validation of the solver is twofold. First, it is of great importance to ensure that the overall coupling of the fluid-structure interaction problem is executed correctly. Second, a good choice of mesh extrapolation model is essential to avoid divergence of the numerical solution, due to mesh entanglement. Based on experience in section, 4.2.1-2, the finite element pair P2-P1 for the fluid solver, and P2-P2 for the solid solver proved successful. Therefore the finite-elements P2-P2-P1 for deformation, velocity, and pressure are chosen for the numerical experiments. Higher order elements will not be examined, mainly due to long computational time, even for optimized solver approaches.

Solid parameters			
parameter	FSI-1	FSI-2	FSI-3
$\rho^s [10^3 \frac{kg}{m^3}]$	1	10	1
ν^s	0.4	0.4	0.4
$\mu^s [10^6 \frac{kg}{ms^2}]$	0.5	0.5	2.0
Fluid parameters			
$\rho^f [10^3 \frac{kg}{m^3}]$	1	1	1
$\nu^f [10^{-3} \frac{m^2}{s}]$	1	1	1
U	0.2	1	2
parameter	FSI-1	FSI-2	FSI-3
Re	20	100	200

Table 4.10: Fluid-structure interaction sub-problem parameters

Results

The numerical results for FSI-1, FSI-2, and FSI-3 are shown in Table 4.10-12. For all sub-problems, a spatial convergence study has been conducted on three different meshes with increasing resolution, with the relative error of the finest spatial and temporal resolution. For FSI-1 in Table 4.10, an additional option is proposed, omitting mesh moving models from the monolithic variational form from section 3.2.2. A comparison of the validation parameters lift, drag, and displacement with different mesh moving models can be found in Figure 4.2-3. Finally, Figure 4.7 and 4.9 visualize the flow field and deformation of the elastic flag for a given time.

FSI-1

Laplace					
nel	ndof	ux of A [$x 10^{-3}$]	uy of A [$x 10^{-3}$]	Drag	Lift
2474	21249	0.0226	0.8200	14.061	0.7542
7307	63365	0.0227	0.7760	14.111	0.7517
11556	99810	0.0226	0.8220	14.201	0.7609
Reference		0.0227	0.8209	14.295	0.7638
Error		$< 10^{-6} \%$	$< 10^{-6} \%$	0.66 %	0.38 %
Linear Elastic					
nel	ndof	ux of A [$x 10^{-3}$]	uy of A [$x 10^{-3}$]	Drag	Lift
2474	21249	0.0226	0.8198	14.061	0.7541
7307	63365	0.0227	0.7762	14.111	0.751
11556	99810	0.0226	0.8222	14.201	0.7609
Reference		0.0227	0.8209	14.295	0.7638
Error		$< 10^{-6} \%$	$< 10^{-6} \%$	0.66 %	0.38 %
Biharmonic bc1					
nel	ndof	ux of A [$x 10^{-3}$]	uy of A [$x 10^{-3}$]	Drag	Lift
2474	21249	0.0226	0.8200	14.061	0.7541
7307	63365	0.0227	0.7761	14.111	0.7517
11556	99810	0.0227	0.8017	14.205	0.9248
Reference		0.0227	0.8209	14.295	0.7638
Error		$< 10^{-6} \%$	$< 10^{-6} \%$	0.63 %	21.08 %
Biharmonic bc2					
nel	ndof	ux of A [$x 10^{-3}$]	uy of A [$x 10^{-3}$]	Drag	Lift
2474	21249	0.0226	0.8200	14.061	0.7543
7307	63365	0.0227	0.7761	14.111	0.7518
11556	99810	0.0227	0.8020	14.205	0.9249
Reference		0.0227	0.8209	14.295	0.7638
Error		$< 10^{-6} \%$	$< 10^{-6} \%$	0.63 %	21.09 %
No extrapolation					
nel	ndof	ux of A [$x 10^{-3}$]	uy of A [$x 10^{-3}$]	Drag	Lift
2474	21249	0.0224	0.9008	14.064	0.7713
7307	63365	0.0226	0.8221	14.117	0.7660
11556	99810	0.0225	0.8787	14.212	0.7837
Reference		0.0227	0.8209	14.295	0.7638
Error		$< 10^{-6} \%$	$< 10^{-5} \%$	0.58 %	2.61 %

Table 4.11: FSI 1 - Comparison of mesh extrapolation models for three spatial refinements

FSI-2

Laplace $\Delta t = 0.01 \quad \theta = 0.51$					
nel	ndof	ux of A [$x 10^{-3}$]	uy of A [$x 10^{-3}$]	Drag	Lift
2474	21249	-15.27 \pm 13.45	1.34 \pm 82.4	157.00 \pm 14.85	-1.09 \pm 258.47
7307	63365	-14.23 \pm 13.37	1.31 \pm 82.2	159.3 \pm 15.43	0.92 \pm 254.53
11556	99810	-14.96 \pm 13.24	1.28 \pm 81.9	161.07 \pm 17.81	0.02 \pm 256.04
$\Delta t = 0.001 \quad \theta = 0.5$					
nel	ndof	ux of A [$x 10^{-3}$]	uy of A [$x 10^{-3}$]	Drag	Lift
2474	21249	-15.61 \pm 13.21	1.34 \pm 83.6	155.38 \pm 13.98	-3.00 \pm 289.06
7307	63365	-15.31 \pm 13.07	1.02 \pm 82.8	156.81 \pm 14.95	-2.00 \pm 276.24
11556	99810	-15.28 \pm 13.04	1.28 \pm 82.9	158.45 \pm 16.09	-2.53 \pm 276.13
Reference		-14.58 \pm 12.44	1.23 \pm 80.6	208.83 \pm 73.75	0.88 \pm 234.2
Error		(4.8 \pm 4.8) $10^{-6} \%$	(4 \pm 2.8) $10^{-6} \%$	24.1 % \pm 78.1 %	387.5 % \pm 17.9 %

Biharmonic 1 $\Delta t = 0.01 \quad \theta = 0.51$					
nel	ndof	ux of A [$x 10^{-3}$]	uy of A [$x 10^{-3}$]	Drag	Lift
2474	21249	-15.44 \pm 13.24	-1.38 \pm 82.3	157.67 \pm 15.02	-0.89 \pm 258.87
7307	63365	-15.04 \pm 12.96	0.99 \pm 81.9	159.83 \pm 16.83	0.98 \pm 245.40
11556	99810	-15.29 \pm 13.17	1.29 \pm 82.5	161.69 \pm 18.73	-1.86 \pm 251.30
$\Delta t = 0.001 \quad \theta = 0.5$					
nel	ndof	ux of A [$x 10^{-3}$]	uy of A [$x 10^{-3}$]	Drag	Lift
2474	21249	-15.36 \pm 13.12	1.35 \pm 83.1	155.38 \pm 13.74	-2.55 \pm 285.19
7307	63365	-15.23 \pm 12.97	1.03 \pm 82.4	157.14 \pm 15.18	-8.62 \pm 263.87
11556	99810	-15.27 \pm 12.99	1.31 \pm 82.7	157.72 \pm 15.58	3.34 \pm 258.76
Reference		-14.58 \pm 12.44	1.23 \pm 80.6	208.83 \pm 73.75	0.88 \pm 234.2
Error		(4.7 \pm 4.4) $10^{-6} \%$	(6.5 \pm 2.6) $10^{-6} \%$	208.83 \pm 73.75	0.88 \pm 234.2

Biharmonic 2 $\Delta t = 0.01 \quad \theta = 0.51$					
nel	ndof	ux of A [$x 10^{-3}$]	uy of A [$x 10^{-3}$]	Drag	Lift
2474	21249	-14.93 \pm 13.22	1.35 \pm 81.5	157.76 \pm 15.04	-0.49 \pm 254.13
7307	63365	-14.67 \pm 13.05	1.00 \pm 80.9	159.59 \pm 16.77	2.22 \pm 248.11
11556	99810	1.58 \pm 12.86	1.23 \pm 81.5	161.85 \pm 18.84	-1.64 \pm 247.04
$\Delta t = 0.001 \quad \theta = 0.5$					
nel	ndof	ux of A [$x 10^{-3}$]	uy of A [$x 10^{-3}$]	Drag	Lift
2474	21249	-15.63 \pm 12.7	1.31 \pm 82.9	155.55 \pm 13.82	-2.45 \pm 281.18
7307	63365	-14.99 \pm 12.81	0.99 \pm 82.14	156.86 \pm 15.05	-1.65 \pm 269.84
11556	99810	-15.26 \pm 12.91	1.27 \pm 81.8	156.86 \pm 15.05	-1.65 \pm 269.84
Reference		-14.58 \pm 12.44	1.23 \pm 80.6	208.83 \pm 73.75	0.88 \pm 234.2
Error		(4.6 \pm 3.7) $10^{-6} \%$	(3.2 \pm 1.4) $10^{-6} \%$	24.8 % \pm 79.5 %	287.5 % \pm 15.2 %

Table 4.12: FSI 1 - Comparison of mesh extrapolation models for $\Delta t = [0, 0.01, 0, 0.001]$, for three spatial refinements

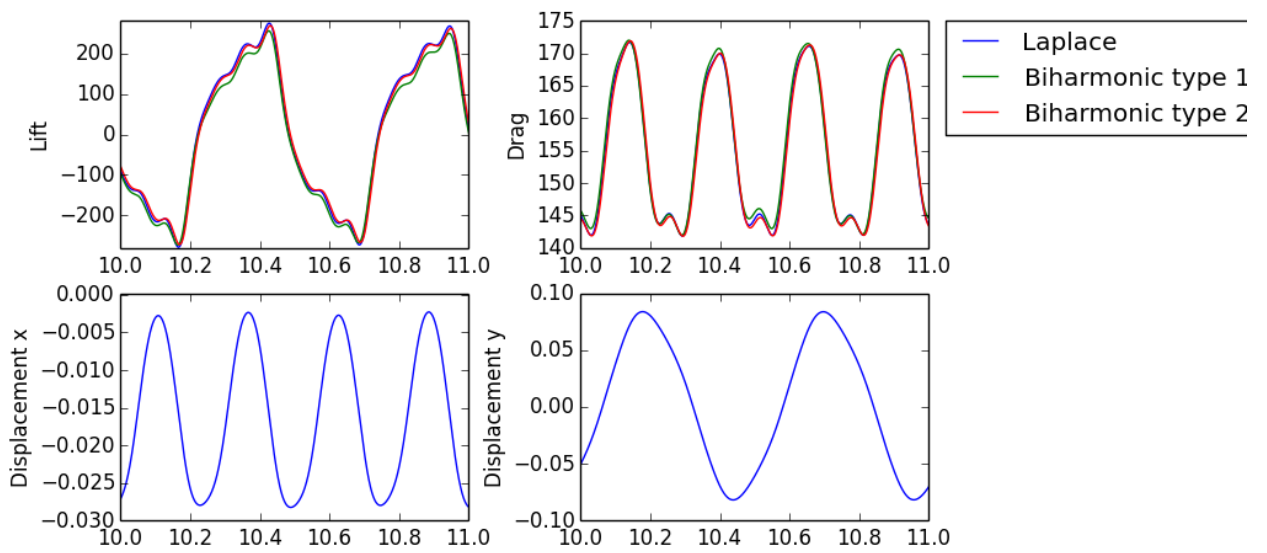


Figure 4.6: FSI-2, visualization of fully developed flow with structure deformation at time $t = 9s$.

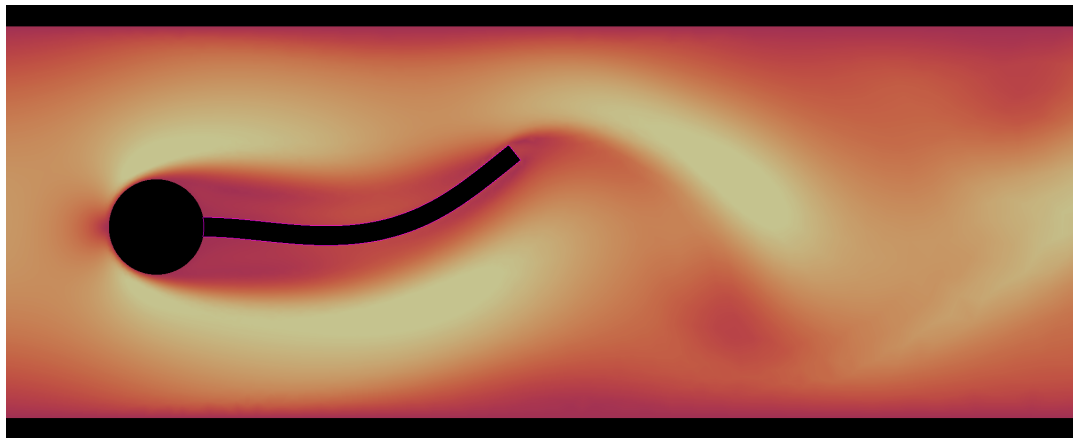


Figure 4.7: FSI-2, visualization of fully developed flow with structure deformation at time $t = 9s$.

FSI-3

Table 4.13: FSI 3 - Comparison of mesh extrapolation models

Laplace $\Delta t = 0.01\theta = 0.51$					
nel	ndof	ux of A [x 10^{-3}]	uy of A [x 10^{-3}]	Drag	Lift
2474	21249	-2.41 \pm 2.41	1.49 \pm 32.21	449.39 \pm 14.72	0.55 \pm 155.80
7307	63365	-2.32 \pm 2.31	1.32 \pm 31.80	451.76 \pm 16.10	1.04 \pm 151.51
11556	99810	-2.34 \pm 2.34	1.59 \pm 31.91	455.94 \pm 17.34	-0.01 \pm 151.36
$\Delta t = 0.001\theta = 0.5$					
nel	ndof	ux of A [x 10^{-3}]	uy of A [x 10^{-3}]	Drag	Lift
2474	21249	-2.91 \pm 2.74	1.28 \pm 35.01	450.90 \pm 18.11	2.28 \pm 161.13
7307	63365	-2.82 \pm 2.66	1.24 \pm 34.69	453.56 \pm 19.80	2.94 \pm 158.67
11556	99810	-2.88 \pm 2.72	1.49 \pm 34.97	458.60 \pm 22.12	2.23 \pm 158.95
Reference		-2.69 \pm 2.56	1.48 \pm 34.38	457.3 \pm 22.66	2.22 \pm 149.78
Error		(7.0 \pm 6.2) 10^{-6} %	(6.7 \pm 1.7) 10^{-6} %	0.28 % \pm 2.38 %	0.45 % \pm 6.12 %

Biharmonic 1 $\Delta t = 0.01\theta = 0.51$					
nel	ndof	ux of A [x 10^{-3}]	uy of A [x 10^{-3}]	Drag	Lift
2474	21249	-2.40 \pm 2.38	1.58 \pm 32.07	450.16 \pm 15.11	-20.09 \pm 148.17
7307	63365	-2.26 \pm 2.14	1.70 \pm 31.3	457.37 \pm 15.24	-51.77 \pm 127.28
11556	99810	-2.33 \pm 2.32	1.93 \pm 31.5	456.40 \pm 17.45	0.45 \pm 149.68
$\Delta t = 0.001\theta = 0.5$					
nel	ndof	ux of A [x 10^{-3}]	uy of A [x 10^{-3}]	Drag	Lift
2474	21249	-2.18 \pm 2.10	3.52 \pm 2.90	435.19 \pm 9.77	-1.59 \pm 151.45
7307	63365	-2.80 \pm 2.64	1.25 \pm 3.45	454.38 \pm 19.76	17.97 \pm 155.08
11556	99810	-2.84 \pm 2.68	1.50 \pm 3.47	459.12 \pm 22.97	-3.12 \pm 171.22
Reference		-2.69 \pm 2.56	1.48 \pm 34.38	457.3 \pm 22.66	2.22 \pm 149.78
Error		(5.5 \pm 4.6) 10^{-6} %	(1.3 \pm 8.9) 10^{-6} %	0.40 % \pm 1.37 %	240.5 % \pm 14.3 %

Biharmonic 2 $\Delta t = 0.01\theta = 0.51$					
nel	ndof	ux of A [x 10^{-3}]	uy of A [x 10^{-3}]	Drag	Lift
2474	21249	-2.33 \pm 2.33	1.57 \pm 31.6	449.44 \pm 14.82	0.80 \pm 152.03
7307	63365	-2.25 \pm 2.23	1.35 \pm 31.3	452.63 \pm 16.29	17.11 \pm 146.05
11556	99810	-2.25 \pm 2.29	1.59 \pm 31.4	457.89 \pm 17.26	57.83 \pm 141.69
$\Delta t = 0.001\theta = 0.5$					
nel	ndof	ux of A [x 10^{-3}]	uy of A [x 10^{-3}]	Drag	Lift
2474	21249	-2.83 \pm 2.66	1.31 \pm 34.5	450.24 \pm 18.25	2.57 \pm 175.42
7307	63365	-2.77 \pm 2.61	0.98 \pm 34.6	453.53 \pm 20.01	2.60 \pm 159.13
11556	99810	-2.80 \pm 2.65	1.37 \pm 34.7	458.41 \pm 22.23	15.56 \pm 157.78
Reference		-2.69 \pm 2.56	1.48 \pm 34.38	457.3 \pm 22.66	2.22 \pm 149.78
Error		(4.0 \pm 3.5) 10^{-6} %	(7.4 \pm 9.3) 10^{-6} %	0.24 % \pm 1.90 %	600.9 % \pm 5.34 %

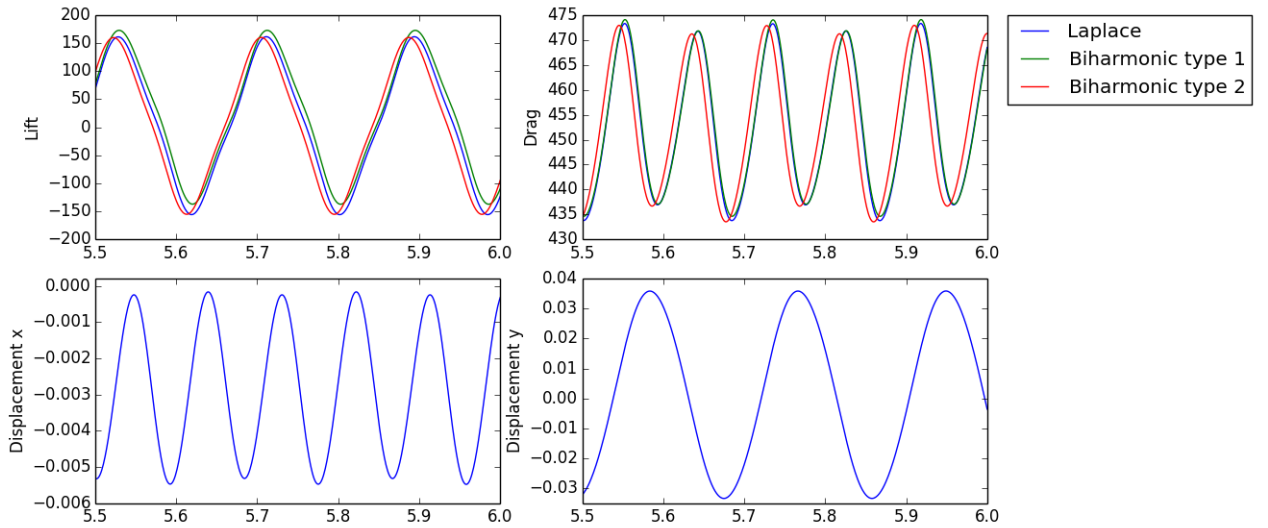


Figure 4.8: Comparison of mesh motion models for FSI-3, in time interval $t \in [5.5, 6]$.

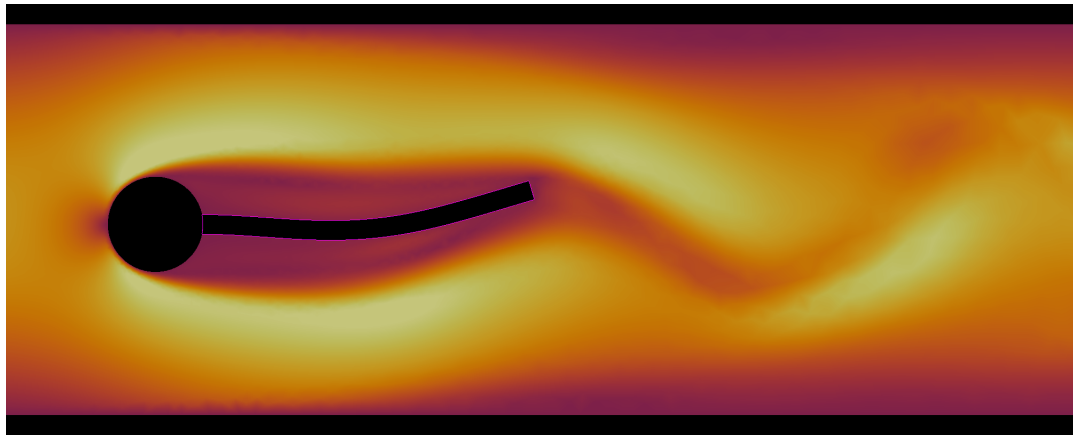


Figure 4.9: FSI-3, visualization of fully developed flow with structure deformation at time $t = 5.1s$.

Discussion

For FSI-1, all models excel well in comparison with the reference solution, even at coarse mesh resolution. Due to low reynolds number flow the induced deformation of the elastic flag is very small, FSI-1 proves to be excellent for initial validation of fluid-structure interaction solvers. However, due the small deformations of the elastic flag of order 10^{-5} , FSI-1 doesn't provide a rigorous test case for mesh extrapolation models. By omitting mesh extrapolation from the variational formulation in section 3.3.2, reasonable results are still obtained in Table 4.10. This fact proves FSI-1 to be misleading in terms of mesh extrapolation model, but remains excellent for initial validation of fluid-structure interaction solvers and the overall coupling of the fluid and solid equations.

The FSI-2 problem proved to be one of the most demanding tests, due to the large deformation of the elastic flag. For large deformations, the chance of fluid mesh entanglement was considerably high, stressing the mesh moving models extensively. The linear elastic model failed for both time sizes, but not due to mesh entanglement but early failure of the Newton-solver. This finding is comparable with the investigation conducted in [30], where early failure of the Newton-solver is in context with long-term simulation of the implicit Crank-Nicolson scheme. In their study, a shifted implicit shifted Crank-Nicolson scheme $\theta = 0.5 + \Delta t$ proved to further improve stability for the newton-solver, making the numerical scheme stable for coarse time-step. Further, numerical investigation in [30] showed that for both Crank-Nicolson and shifted Crank-Nicolson are stable for $\Delta t < 0.003$ for the same benchmark. In my study, both implicit schemes was applicable for all mesh moving models, except the linear elastic model.

In general, the numerical solution regarding deformation of the elastic flag proved accurate in accordance with the reference solution for all sub-problems. However, the evaluation of drag and lift proved challenging for the periodic FSI-2 and FSI-3 problems. For FSI-2, poor accuracy was observed for all mesh resolutions and time steps, while for FSI-3 the evaluation of drag remained accurate. The same observations was found in [42], a followup work of the original benchmark [16], where numerical solutions committed by different research communities was compared. The diversity of lift and drag values provided by different research communities was surprising, as differences of order 50% for drag and lift values, and 10% for displacement was observed. More surprisingly was that the authors of the original benchmark [16], who also committed their numerical results, didn't match their own reference solution with the same solver. Therefore, comparison of lift and drag forces with the reference solution alone can be misleading, and should not be the main acceptance criteria for code validation for this benchmark. Given the remarks in [42], the comparison of deformation is arguably a better main acceptance criteria. On this basis, the FSI code is validated in accordance with the original benchmark.